ADVANCED FUNCTIONAL MATERIALS
www.afm-journal.de

Materials Views
www.MaterialsViews.com

# Substantial Recoverable Energy Storage in Percolative Metallic Aluminum-Polypropylene Nanocomposites

*Lisa A. Fredin, Zhong Li, Michael T. Lanagan,* Mark A. Ratner,* and Tobin J. Marks**

**Chemisorption of the activated metallocene polymerization catalyst derived from [*rac*-ethylenebisindenyl]zirconium dichlororide (EBIZrCl$_2$) on the native $Al_2O_3$ surfaces of metallic aluminum nanoparticles, followed by exposure to propylene, affords 0–3 metal-isotactic polypropylene nanocomposites. The microstructures of these nanocomposites are characterized by X-ray diffraction, transmission electron microscopy, scanning electron microscopy, and atomic force microscopy. Electrical measurements show that increasing the concentration of the filler nanoparticles increases the effective permittivity of the nanocomposites to $\varepsilon_r$ values as high as 15.4. Because of the high contrast in the complex permittivities and conductivities between the metallic aluminum nanoparticles and the polymeric polypropylene matrix, these composites obey the percolation law for two-phase composites, reaching maximum permittivities just before the percolation threshold volume fraction, $v_f \approx 0.16$. This unique method of *in situ* polymerization from the surface of metallic Al particles produces a new class of materials that perform as superior pulse-power capacitors, with low leakage current densities of $\approx 10^{-7}$–$10^{-9}$ A/cm$^2$ at an applied field of $10^5$ V/cm, low dielectric loss in the 100 Hz–1 MHz frequency range, and recoverable energy storage as high as 14.4 J/cm$^3$.**

## 1. Introduction

For next-generation high energy density pulsed-power and power capacitors[1,2] it is essential to develop dielectric materials with high dielectric permittivity, high breakdown strength, low loss, and fast response.[3] Metal particle-based dielectric materials typically have very high permittivities and low working voltages; however, such materials are difficult to process into multilayer thin films[4] without the use of high temperature sintering.[5] In contrast, the low permittivities of typical polymer dielectrics limit their applications scope, despite their good dielectric strength and facile processability.[6] Inorganic–polymer nanocomposite materials[3a,7] have recently attracted intense research attention since they combine the best properties of both phases, yielding potential aggregate performance well beyond that of each individual constituent material.[8] While metals are not typically considered to be dielectric materials themselves, at low frequencies the plasma frequency of the metallic electron gas is much greater than the electromagnetic propagation frequency, leading to an almost purely imaginary complex permittivity, which is proportional to the real-valued electrical conductivity.[9] Whereas ferroelectrics have a large real part of the complex permittivity, metals have a large imaginary part, both of which lead to low impedance. When these low impedance phases are included in an insulating polymer matrix they are expected to lead to high capacitance and high local fields in the low permittivity matrix phase.[10] Many types of ceramic oxide particles having high permittivity have been dispersed in polymer matrices to form 0–3 composites (this notation indicates a zero-dimensional structure, e.g., spheres, in a three-dimensional matrix). These composites are not only processable but have been shown to have impressive permittivies[11] and moderate stored energies.[12]

Typically inorganic–polymer 0–3 nanocomposites[10] are synthesized via conventional solution mixing[13] or mechanical blending methods,[5] resulting in agglomerated nanoparticles and high levels of phase separation. Such inhomogeneous films lead to high dielectric loss and low dielectric strength. Adding surfactants during processing[14] or covalently grafting the polymer chains to inorganic nanoparticle surfaces by either traditional[15] or new synthetic means[3b] have been also been investigated to enhance the nanoparticle dispersion in the host polymer, with varying degrees of success. An alternative approach to dielectric composites that we have recently demonstrated, *in situ* polymerization, affords an effective, straightforward, and low cost means of dispersing oxide nanoparticles in polyolefin matrices.[7a,12a,16]

In a process inspired by the fate of $SiO_2$ catalyst supports in heterogeneous or slurry olefin polymerizations, where the very large local hydrostatic pressures arising from the propagating

L. A. Fredin, Dr. Z. Li, Prof. M. A. Ratner, Prof. T. J. Marks
Department of Chemistry and the Materials Research Center
Northwestern University
Evanston, IL 60208-3113, USA
E-mail: ratner@chem.northwestern.edu; t-marks@northwestern.edu
Prof. M. T. Lanagan
Center for Dielectric Studies
Materials Research Institute
The Pennsylvania State University
University Park, PA 16802-4800, USA
E-mail: mxl46@psu.edu

DOI: 10.1002/adfm.201202469

polyolefin chains induce $SiO_2$ particle fracture,[17] *in situ* polymerization of polyolefin chains from surfaces within a catalyst-impregnated nanoparticle disrupts particle agglomeration to yield a randomly dispersed, relatively homogeneous nanocomposite film.[16a] Thus, methylalumoxane (MAO)-activated single-site metallocene catalysts[18] supported on oxide nanoparticles have been employed to prepare extensive series of 0–3 composites with ceramic $BaTiO_3$, $TiO_2$, $ZrO_2$, yttria-stabilized $ZrO_2$, $SrTiO_3$, $Ba_{0.5}Sr_{0.5}TiO_3$, and MgO nanoparticle fillers dispersed in polyolefin matrices (polypropylene of varying tacticities, polyethylene, polystyrene, and various olefin copolymers).[7a,12a,16b,c] The resulting materials can have both high effective permittivities and high dielectric breakdown metrics.[7a,12a,16a,b] Furthermore, the polymerization cocatalyst, MAO, leaves a thin (≈ 0.5 nm) residual $Al_2O_3$ shell on the nanoparticles, which has the beneficial effect of grading the large permittivity contrast between the nanoparticles and the polyolefin matrix.[16b,19]

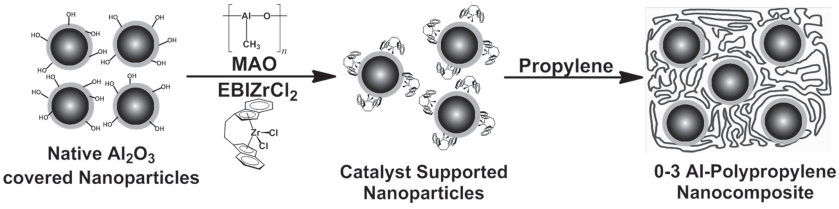


**Figure 1.** Schematic of 0-3 polypropylene nanocomposite synthesis process.

We previously reported that the permittivities of metal-oxide polypropylene composites with extremely high dielectric constant nanoparticles ($BaTiO_3$ $\varepsilon_r > 2000$) were well explained by two-phase polymer composite percolation theory.[16b] The high impedance contrast between the filler and matrix means that the low impedance phase is conductive compared to the insulating matrix. According to polymer composite percolation theory, the permittivity of conductor-insulator composites follows a volume fraction power law and exhibits an abrupt decline past the percolation threshold.[20] This follows, since at high volume fractions the average distance between nanoparticles is smaller and the polymer expanse separating the nanoparticles becomes thinner, making the composite behave like a percolated system. The theory prediction for the effective permittivity before the percolation threshold is given by **Equation 1**:

$$\varepsilon_{eff} = \varepsilon_m \left| \frac{v_c - v_f}{v_c} \right|^{-q} \quad (1)$$

where $\varepsilon_m$ is the permittivity of the matrix, $v_f$ is the filler volume fraction, $v_c$ is the percolation threshold, and $q$ is the critical exponent which is a fit parameter.[21] If the inclusion phase particles are spherical and similar in size to the matrix phase, then a random distribution of inclusions will have a percolation threshold at ≈16 vol%.[5b,22] This percolation threshold has been used effectively in our previous studies of similar *in situ* polymerized composites with particles having permittivities greater than 1000, such as $BaTiO_3$,[16b] and for other polymer composites containing high permittivity (>1000) phases.[23] Note that larger filler particle sizes, non-spherical particle shapes, and nanoparticle agglomeration can result in lower percolation thresholds.[24]

In the present study, we extend the *in situ* polymerization approach to oxide-coated metallic nanoparticles. We investigate the dielectric and energy storage properties of the resulting nanocomposites as well as the degree to which they conform to percolation behavior (Equation 1). Synthetically, we bind a metallocene precatalyst, [*rac*-ethylenebisindenyl]-zirconium dichloride ($EBIZrCl_2$) to the ≈2 nm thick (≈1% by volume)[22,25] native oxide coating of Al nanoparticles. We have confirmed this thickness on the present nanoparticles by transmission electron microscopy (TEM). Note that this oxide thickness is comparable to that of a single $Al_2O_3$ layer derived from exposing methylaluminoxide (MAO) to air as used in our previous studies of ceramic nanoparticle-polyolefin composites.[7a,12a,16b] The chemisorbed[16c,17a,18b,c,e,26] $EBIZrCl_2$ is then activated with the aluminum alkyl co-catalyst, MAO[19,26c] for the *in situ* synthesis of isotatic polypropylene-aluminum nanoparticle composites (**Figure 1**). The microstructures of these materials are characterized by X-ray diffraction, TEM, scanning electron microscopy (SEM), and atomic force microscopy (AFM). Capacitors are then fabricated with these nanocomposites and are characterized experimentally by a full range of electrical measurements, and theoretically using two-phase polymer composite percolation theory. It will be seen that these nanocomposites closely obey the percolation law for two-phase composites, reach maximum permittivities just before the percolation threshold volume fraction, $v_f \approx 0.16$, and perform well as capacitor materials, with resistivities of $\approx 10^{12}$–$10^{15}$ Ω·cm, low dielectric loss in the 100 Hz–1 MHz frequency range, and have impressive recoverable energy storage as high as 14.4 J/cm$^3$.

## 2. Results

Here we discuss the fabrication and electrical characterization of a series of Al-$^{iso}$PP nanocomposites ranging in Al content from 0.7% to 40%. The synthesis, composition, and microstructure of these nanocomposites are confirmed by elemental analysis, TEM, SEM, and AFM, followed by the fabrication of capacitors. Next, the capacitance, leakage current, dielectric loss, and polarization of each composite are measured. From these data, the permittivity, leakage current density, and dielectric loss at low frequencies and low fields, as well as the recoverable energy storage, efficiency of energy stored, and effective permittivity at high fields are extracted for each composite in the series.

### 2.1. Synthesis of Metal-Polypropylene Nanocomposites

The native $Al_2O_3$-covered Al nanoparticles were exposed to solutions of the metallocene precatalyst $EBIZrCl_2$ and then to the MAO co-catalyst, forming supported polymerization-active surface species.[27] Subsequent *in situ* polymerization of propylene yields the metal nanoparticle-polyolefin nanocomposites. These nanocomposites consist of three intimately dispersed components: 1) low impedance metal nanoparticles, 2) a medium impedance native $Al_2O_3$ shell, and 3) an insulating isotactic

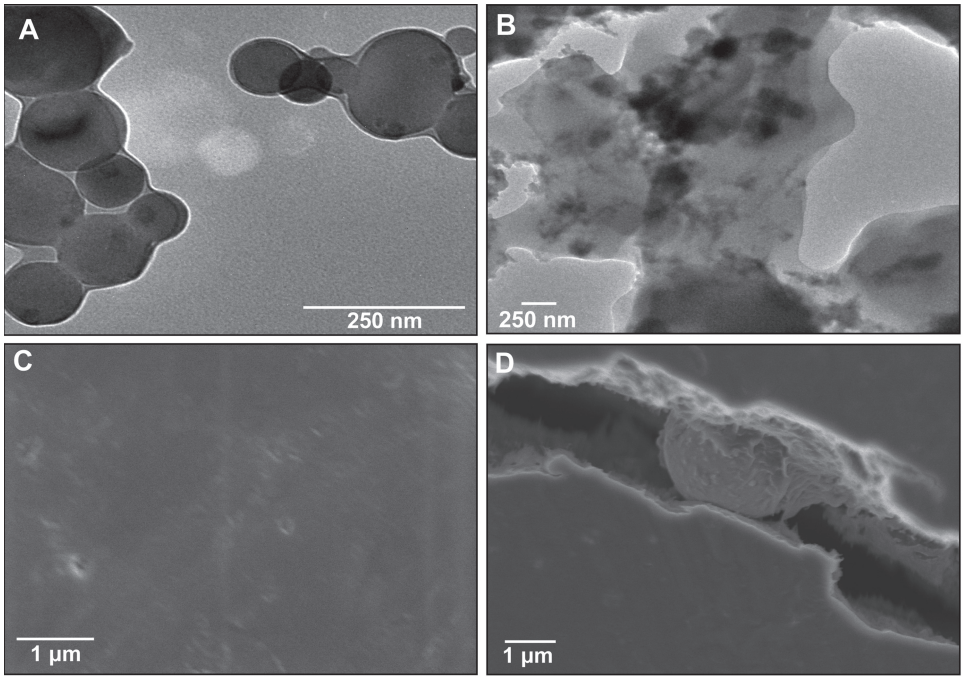


**Figure 2.** TEM images of A) Al nanoparticles, B) 10.4% Al-*iso*PP composite, and C) the sample surface SEM image for Al-*iso*PP thin film with 10.4% loading, fabricated by hot-pressing. The thin film has 2.6 nm RMS roughness by AFM. Note the cracks in the films having higher nanoparticle loading fractions as shown for D) a 38.2% loading sample.

polypropylene matrix. By controlling the polymerization time, the Al–$^{iso}$PP [this notation has the format, nanoparticle identity-polymer matrix] nanoparticle volume fractions were varied over the range 0.007 to 0.408.

As shown in previous studies, the $C_2$–symmetric metallocene catalyst EBIZrCl$_2$ produces highly isotactic ([*mmmm*] = 83%) and crystalline (monoclinic $\alpha$ phase) polypropylene.[16c] Thus, TEM images of the present polypropylene nanocomposites (**Figure 2**b) clearly show that the nanoparticles are embedded and dispersed in the polymer matrix with more particles in close proximity at higher volume fractions. X-ray diffraction (XRD) and TEM images of the analogous ceramic-nanocomposites confirmed the uniform dispersion of particles using this *in situ* polymerization method.[7a,12a,16] While the metallic particles dominate the XRD spectra (making any X-ray analysis of the polymer composite microstructure difficult), the present metallic nanocomposites show dispersion and microstructure in the SEM and TEM very similar to that of their ceramic counterparts.[7a,16] Indeed, TEM is the optimal technique for this analysis.[16a,b,28] Generally, samples with lower nanoparticle loadings have better dispersion. The pronounced structural homogeneity of the nanocomposites is also confirmed by the uniformity of the films (SEM) fabricated by hot-pressing (Figure 2c) and by the low surface RMS roughnesses (2–3 nm) measured by AFM.

### 2.2. Nanocomposite Properties in Low Electric Fields

Effective permittivity data for the present nanocomposites derived from capacitance measurements are compiled in **Table 1**. Generally, for those Al-$^{iso}$PP nanocomposites below the percolation threshold, the effective permittivity increases as the filler volume fraction increases. For all the Al-$^{iso}$PP nanocomposites, the films look and feel metallic, and because of this, the higher loading films are brittle and crack easily.

The permittivities of the Al–$^{iso}$PP nanocomposite films were also characterized as a function of frequency (**Figure 3**). In the 100 Hz to 1 MHz range, the dielectric permittivity increases as

**Table 1.** Dielectric properties of metal-isotactic polypropylene nanocomposites having different volume fractions of Al nanoparticles in the polymer matrix.

| Al particle vol%[a)] | Permittivity[b)] | Interparticle distance[c)] [nm] |
|---|---|---|
| 0.7% | 2.4 ± 0.4 | 321.3 |
| 2.0% | 2.8 ± 0.9 | 196.9 |
| 2.9% | 3.0 ± 0.4 | 162.3 |
| 10.4% | 10.5 ± 0.3 | 71.4 |
| 12.4% | 15.4 ± 0.1 | 61.6 |
| 25.4% | conductive[d)] | 27.3 |
| 38.2% | conductive | 11.1 |
| 40.8% | conductive | 8.7 |

[a)]From elemental analysis; [b)]Derived from capacitance measurements on 5 devices fabricated with at least 2 different thin films; [c)]Calculated from **Equation 3**; [d)]Samples with vol% higher than the percolation threshold were so conductive that their measured capacitance was not applicable.

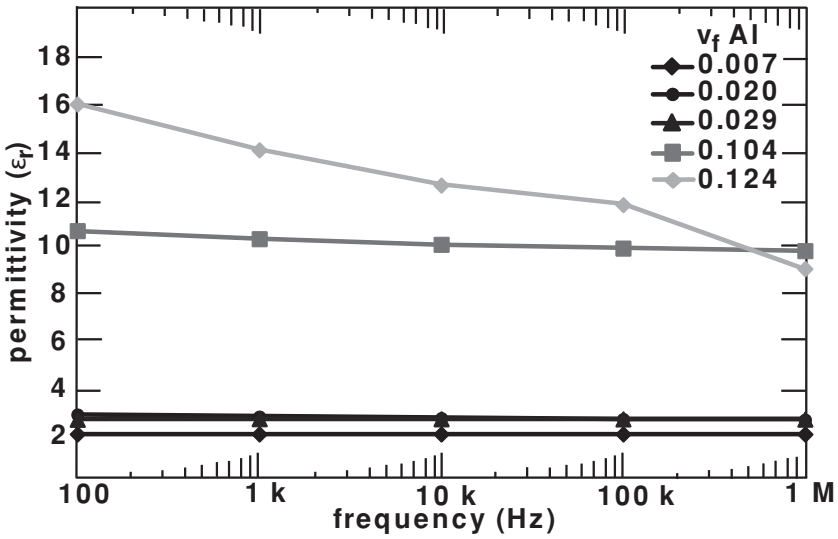


**Figure 3.** Permittivity of Al-$^{iso}$PP nanocomposites over the frequency range of 100 Hz to 1 MHz.

the nanoparticle loading increases until the loading reaches the critical 0.16 volume fraction, at which point permittivity is no longer an accurate way to characterize these more conductive samples. For the samples with low nanoparticle loadings, the dielectric permittivities vary little with frequency while the samples with higher nanoparticle loadings exhibit falling dielectric permittivity with increasing frequency.

Nanocomposite percolation theory states that as the particle density in the matrix increases, the probability of close nanoparticle-nanoparticle proximity increases, thereby creating elongated dipole moments across multiple particles, and inducing large local fields in the surrounding matrix, resulting in very large increases in overall effective permittivity.[20,21] However, beyond a critical compositional percolation threshold, 16% for a two-phase system with spherical fillers,[5b,22] the permittivity dramatically falls to the level of the matrix or even below if there is damage to the matrix around the fillers resulting from the very large local fields.[29] This can easily be seen in **Figure 4** where the experimental permittivity values for the Al-$^{iso}$PP nanocomposites clearly lie on the fitted percolation line before and approaching the 0.16 threshold. In contrast, the very high volume fraction composites have sufficient Al particles to exhibit appreciable electrical conductivity, indicating a continuous pathway of particles from one electrode to the other. The variation of experimental permittivity for these Al–$^{iso}$PP nanocomposites can be fit to the percolation law with $v_c = 0.16$, resulting in $q = 1.325$, as can be seen in **Figure 5**.

The leakage current densities of the present nanocomposite films with low nanoparticle volume fractions ($v_f < 0.16$) generally fall within the range $10^{-7}$–$10^{-9}$ A/cm$^2$ in an applied electric field of $10^5$ V/cm (**Figure 6**). At the low loading levels ($v_f < 0.16$), the leakage currents decrease with increasing loading. However, for volume fractions past the percolation threshold, the leakage current densities do not follow a specific trend but still remain below $10^{-7}$ A/cm$^2$. The resistivity of these composites calculated from the *I–V* characteristics are $10^{12}$–$10^{17}$ Ω·cm. Thus, the present metallic nanocomposites are excellent insulators below the percolation threshold.

Ideally, for a capacitor that will be continuously charged and discharged, dielectric losses should be as low as possible since losses decrease the amount of energy that can be stored and retrieved from the capacitor over time. As can be seen in **Figure 7**, the present Al-polyolefin nanocomposites exhibit low dielectric loss, less than 0.1 across the 100 Hz–1 MHz range below the percolation threshold. Furthermore, note that the dielectric loss increases significantly when the nanoparticle volume fraction approaches the $v_f = 16\%$ percolation threshold.

### 2.3. Nanocomposite Capacitive Properties in High Electric Fields

To determine nanocomposite dielectric loss at high fields, sample polarization was measured as a function of electric field. The energy density stored in a dielectric material is equal to the integral $U = \int E dD$, where E is the electric field

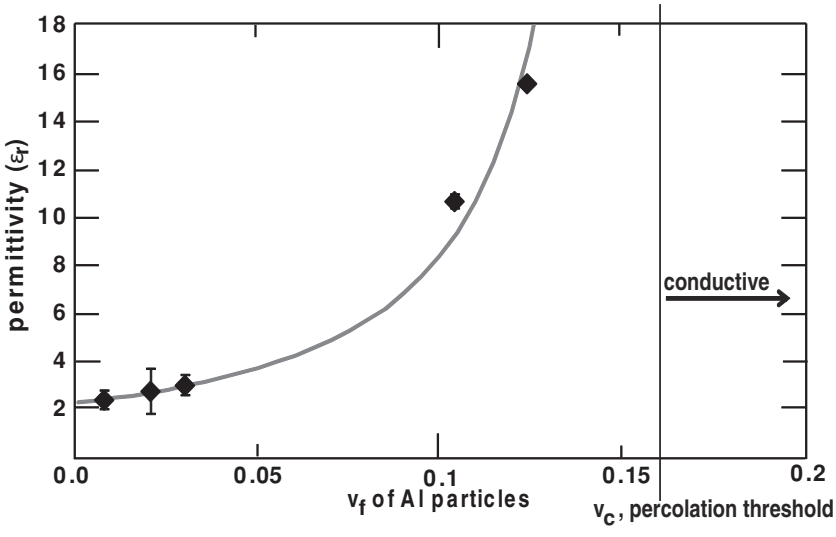


**Figure 4.** Experimental permittivity for Al–$^{iso}$PP nanocomposites as a function of Al nanoparticle volume fraction. Note: each permittivity is calculated from average capacitance measurements on at least 5 devices on at least 2 different thin films; error bars are included for each point, and the solid line is the precolation theory (Equation 1) fit (see Figure 5 for how fit is preformed) for the composites below the critical threshold.

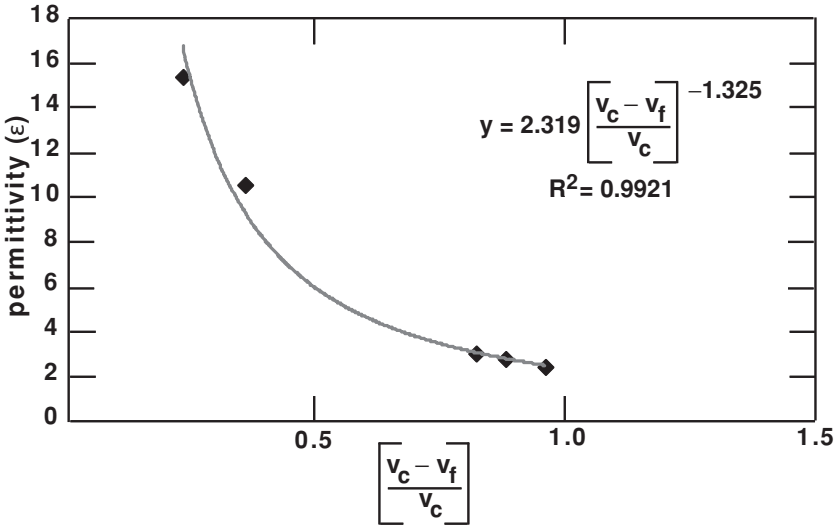


**Figure 5.** Fit of the nanocomposite permittivity to the percolation ratio as expressed in Equation 1. Here $v_c$ is the percolation ratio and $v_f$ is the nanoparticle volume fraction of the sample. By using this fit, the coefficient $\varepsilon_m = 2.319 \pm 0.056$ is derived as the value for the matrix permittivity with a critical exponent q of $1.325 \pm 0.068$.

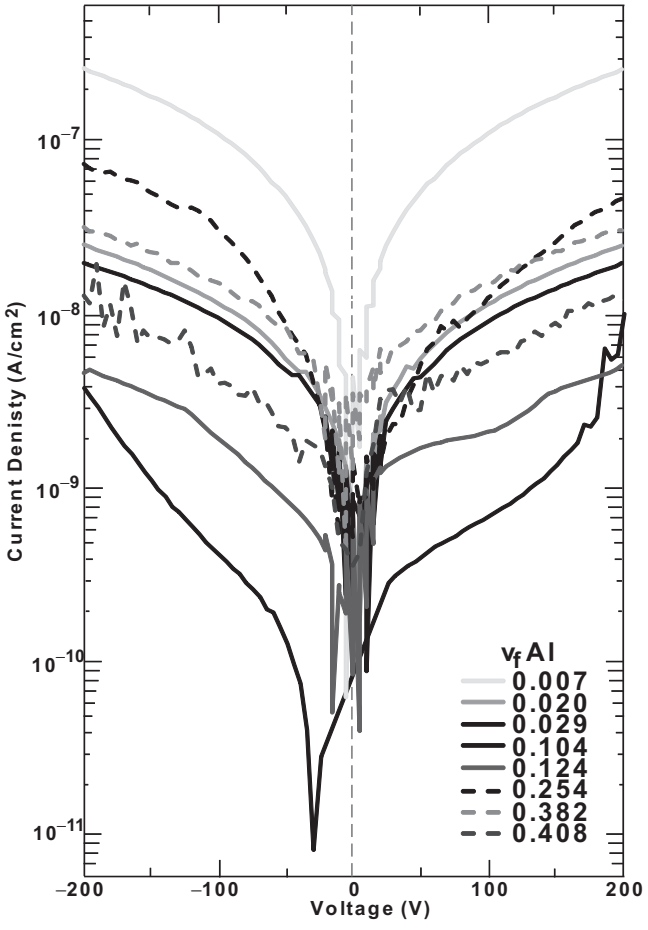


**Figure 6.** Leakage current of Al-$^{iso}$PP nanocomposites having the indicated nanoparticle volume fractions.

and D is the electric displacement. Polarization response "loops" (**Figure 8**) can be related to the stored energy capacity and loss, where the recoverable energy storage is the area above each loop and the loss is the area within each loop (Supporting Information Figure S1).[7a,12a–c,30] These loops are measured by applying increasing fields to the capacitor and observing the amount of charge stored and released. The high field loss, $\Gamma$, can be found from the ratio of energy density recovered to the energy stored (**Equation 2**, graphically depicted in the Supporting Information):

$$\Gamma = \frac{U_{lost}}{U_{stored}} = \frac{U_{stored} - U_{recoverable}}{U_{stored}} \quad (2)$$

At high fields (>40 MV/m), the dielectric loss, $\Gamma$, is less than 25% for samples below $v_f$ = 10.4%; however, the 12.4% composite has a loss of 73%. Furthermore, note that composites with volume fractions above 16% breakdown at voltages below 100 V, and therefore the polarization of these samples is below the instrumental noise level.

There is a clear change in the conduction of the nanocomposites when the applied field is larger than 50 MV/m (Figure 8). For the composites below the percolation threshold the majority of the electric field is thought to arise from local fields within the polymer matrix. From a purely geometric picture of the composite, assuming a spherical shape for the particles and a uniform size distribution and dispersion, the interparticle distance, $l$, can be expressed as in **Equation 3**[31] where $r$ is the average radius of the particles (100 nm Al) and $v_f$ is the volume fraction.

$$l = 2r\left[\left(\frac{\pi}{6v_f}\right)^{1/2} - 1\right] \quad (3)$$

In the 10.4% Al composite, the particles are ≈74 nm apart (all calculated interparticle distances are listed in Table 1), implying that the field in the polymer is essentially double the applied field (≈100 MV/m). This is 1/10 the electric field that Boggs reported for the onset of nonlinear conduction in unfilled polypropylene films.[9]

From each of the polarization loops, the energy stored and the energy recovered can be calculated. This allows extraction of the apparent sample dielectric constant (**Figure 9**) at each applied field. Because the dielectric constant of the metallic Al nanoparticles is complex, it is impossible to extract the exact high field dielectric constant, and thus the energy stored, via the standard expression of **Equation 4**,[32] where $E_{breakdown}$ is the field just before the sample undergoes irreversible breakdown. Note however that the stored energy (recoverable and non-

$$U_{stored} = {}^1\!/_2\,\varepsilon_r\varepsilon_0(E_{breakdown})^2 \quad (4)$$

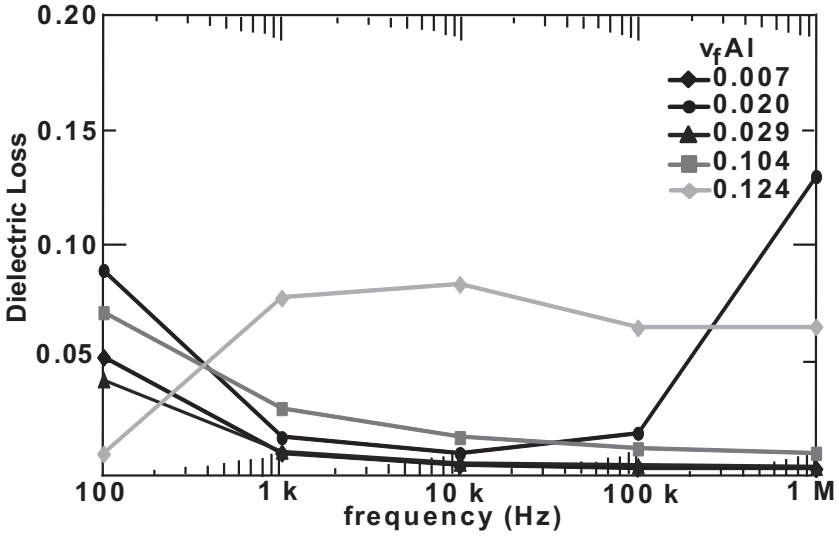


**Figure 7.** Dielectric loss of Al-*iso*PP nanocomposites as a function of Al nanoparticle volume fraction at frequencies from 100 Hz to 1 MHz, and having the indicated nanoparticle volume fractions.

recoverable) can be determined from the polarization loops, and the apparent high field dielectric constant can then be calculated from the non-recoverable energy stored and the breakdown field using **Equation 4**. The energy stored, recoverable energy stored, and calculated high field dielectric constants for the 12.4% Al-composite are summarized in **Table 2**. The calculated high field permittivities are two orders of magnitude higher than the low field measured permittivity; however, they are in the range of other metal composite films.[28a,33] From the polarization loops shown in **Figure 10** it is obvious that as the Al nanoparticle loading increases, the composites exhibit increasing loss just before breakdown (summarized in **Table 3**).

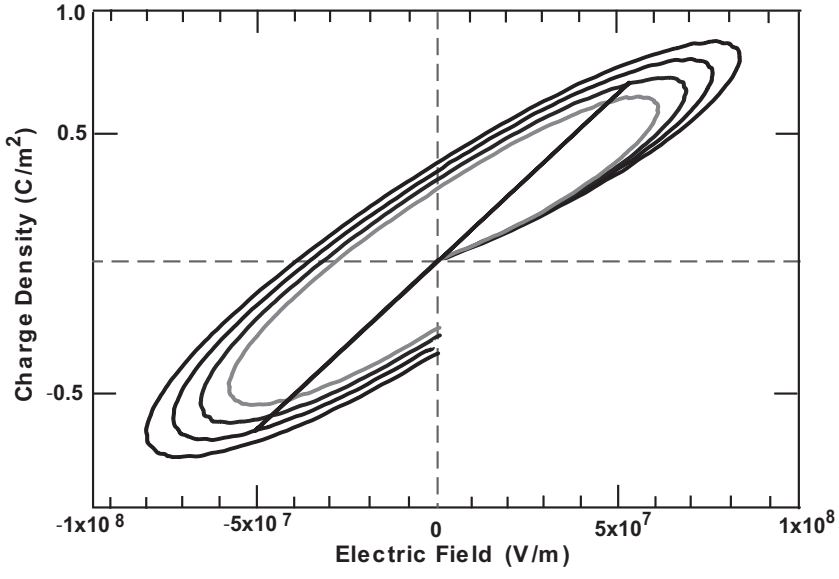


**Figure 8.** Polarization loops for a representative $v_f$ = 12.4% Al-*iso*PP nanocomposite at increasing applied fields.

## 3. Discussion

### 3.1. Synthesis of Metal-Polypropylene Nanocomposites

It is known that nanoparticle agglomeration and phase separation between hydrophilic metal oxides and hydrophobic polymers can compromise nanocomposite electrical properties, resulting in increased electrical leakage and local dielectric breakdown.[34] During the present *in situ* polymerization process, the growing polyolefin chains produce very high local hydrostatic pressures such that the propagating polymer chains efficiently disrupt the nanoparticle agglomerization and afford good nanoscale dispersion, as indicated by TEM and SEM images. Generally, samples with lower nanoparticle loadings are found to have better dispersion. In contrast, nanocomposite films prepared by simple physical mixing of the two constituents typically exhibit large cracks, voids, and pinholes,[14b] all of which are minimized in the present nanocomposite films. Adding surfactant during composite processing is another proven strategy to enhance dispersion and film quality, however residual surfactant can also lead to high leakage currents and dielectric loss.[34] The *in situ* polymerization approach avoids this complication.

### 3.2. Nanocomposite Properties in Low Electric Fields

Previous studies on nanoparticle-polymer composites have suggested that at high filler loadings, the dielectric permittivity may decrease due to imperfect filler packing, and that there is some nanofiller agglomeration, leading to decreased total effective particle-filler interfacial area, hence reduced interfacial polarization.[16,35] Also, lower permittivity at higher frequencies indicates greater space charge and has been observed in other polymer-ferroelectric ceramic composites.[16b,36] At high filler volume fractions, the average interparticle distance is smaller, and the polymer expanse separating the nanoparticles becomes thinner, which will ultimately cause percolative behavior, as direct pathways for charge transport from one electrode to the other emerge.[20a–c,37]

In all of the present electrical characterizations it is clear that nanocomposite samples having a nanoparticle volume fraction less than 16% have well-behaved properties, and that samples with vol% greater than 16% have poor, inconsistent dielectric properties. While the leakage current densities measured are fairly low; for composites where the

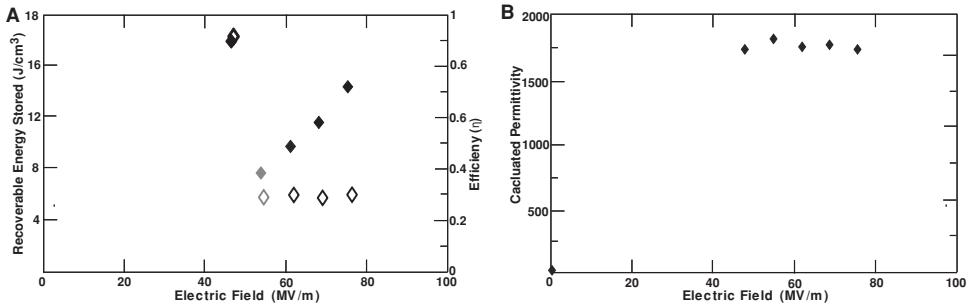


**Figure 9.** A) Recoverable energy stored and efficiency of energy stored for the indicated applied fields, corresponding to the polarization loops in **Figure 8** and B) calculated permittivity from the total energy stored at varying applied fields.

**Table 2.** Apparent high field dielectric constants at varying applied fields for a 12.4% Al-*iso*PP nanocomposite.

| Applied Field [MV/m] | Energy Stored[a] [J/cm$^3$] | Recoverable Stored Energy[b] [J/cm$^3$] | High Field Dielectric Constant[c] |
|---|---|---|---|
| 0 | n/a | n/a | 15.4 |
| 47.8 | 17.5 | 16.7 | 1729 |
| 55.0 | 24.2 | 7.1 | 1810 |
| 62.1 | 29.8 | 9.1 | 1749 |
| 68.8 | 37.0 | 10.8 | 1765 |
| 75.8 | 44.0 | 13.4 | 1729 |

[a]Derived from areas inside and above polarization loops, depicted graphically in Supporting Information Figure S1;[b]Derived from areas above the polarization loop with the highest breakdown field, depicted graphically in Supporting Information Figure S1;[c]Calculated dielectric constant from energy stored using **Equation 4**.

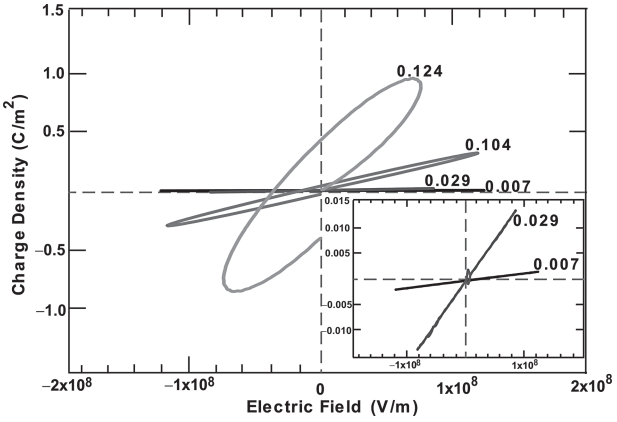


**Figure 10.** Highest polarization measured for Al-*iso*PP nanocomposites having the indicated nanoparticle volume fractions. The inset shows the lower volume fraction polarizations in an expanded scale.

nanoparticle volume fraction is above the $v_f = 16\%$ percolation threshold, the dielectric loss increases dramatically, indicating that the measured capacitance is unreliable and the composites are actually conductive with a percolative path of particles extending from one electrode to the other.

### 3.3. Nanocomposite Capacitive Properties in High Electric Fields

The threshold field inside the polymer matrix appears to be ≈100 MV/m, above which the capacitor has increased percolation pathways creating a non-linearity in the field response. This change in the polarization response above 50 MV/m corresponds to an increase in percolative paths within the sample, and these paths develop at lower applied fields for higher volume fractions. This regime is evident in the open polarization loop at lower field for the 12.4% Al sample (**Figure 10**), and the 10× lower threshold fields than reported in unfilled polypropylene films.[9] The increased high field loss with increasing nanoparticle volume fraction observed here is indicative of increasing space charge and "soft" electrical breakdown.[38] For $v_f < 0.16$, the leakage current density and dielectric loss remain very low while the permittivity increases exponentially with volume fraction, yielding the best performing capacitors of the series at $v_f \approx 10\%$. While the 12.4% Al-capacitor has relatively high loss, the 10.4% Al-capacitor has loss at its breakdown field, 24% loss at ≈120 MV/m, comparable to other low -loss polymer and polymer composite systems[39] including capacitor-optimized biaxally oriented PP films which have a breadown field loss of ≈17%.[40]

These capacitors achieve remarkable high recoverable energy storage densities, with a best performing capacitor storing 14.4 J/cm$^3$ with 76% efficiency (24% loss). This usable energy could be improved by utilizing previously proven polymer processing techniques (e.g., biaxial stretching). These optimized films are expected to yield lower mechanical and defect derived loss resulting in more reliable devices for long term use.[40,41]

## 4. Conclusions

In this study, we report a series of metallic Al nanoparticle-isotactic polypropylene composite dielectrics, the electrical characteristics of which can be accurately described using percolation theory. Because of the *in situ* propylene polymerization by single-site catalyst molecules anchored to the oxide-coated nanoparticles, the nanocomposites produced are well-dispersed in the

**Table 3.** Breakdown voltage and high-field loss characterization of selected Al-polypropylene nanocomposites as a function of the Al nanoparticle volume fraction.

| Al particle vol%[a)] | Breakdown Field[b)] [MV/m] | Thickness [μm][c)] | Dielectric Loss [$I$][d)] | Recoverable Stored Energy[e)] [J/cm$^3$] |
|---|---|---|---|---|
| 0.7% | 123.7 | 9.4 | 0.01 | 0.10 |
| 2.9% | 85.2 | 9.3 | 0.07 | 0.54 |
| 10.4% | 119.3 | 7.0 | 0.24 | 14.4 |
| 12.4% | 75.8 | 10.0 | 0.70 | 13.4 |

[a)]From elemental analysis; [b)]Highest breakdown field measured; [c)]Measured with Veeco Dektak 150 surface profiler; [d)]Derived from area inside polarization loops, depicted graphically in Supporting Information Figure S1; [e)]Maximum recoverable energy storage capacity derived from area above the polarization loop with highest breakdown field, depicted graphically in Supporting Information Figure S1.

polyolefin matrix with no obvious microstructural defects that might lead to poor film performance. This combination of good morphology and extremely low impedance phases (the metallic particles) produces materials that obey percolation theory, not having typical deviations due to defects. The predicted and experimentally realized high permittivities are obtained for volume fractions greater than 10% and less than 16%. This category of metallic particle-polymer composites affords materials that can be fabricated similarly to traditional polymer capacitors while obtaining higher energy storage capacities. Such nanocomposites, with high permittivities, low dielectric losses, and small sensitivities of permittivity and dielectric loss to frequency, are attractive for physically small capacitors having large energy storage capacities and high voltage ratings. Here we demonstrate a series of proof-of-principle Al-*iso*PP composites having permittivities up to 15.4. A capacitor exhibiting particularly good performance has a dielectric permittivity of 10.4, leakage less than $10^{-8}$ A/cm$^2$, resistivity greater than $10^{13}$ Ω•cm, dielectric loss less than 10% at 1 V and below 1 MHz, and 24% at >1 kV and 500 Hz. Moreover, this material has a remarkable 14.4 J/cm$^3$ recoverable energy storage capacity.

## 5. Experimental Section

*Materials and Methods*: All manipulations of air-sensitive materials were performed with rigorous exclusion of oxygen and moisture using Schlenk techniques, or interfaced to a high-vacuum line ($10^{-6}$ Torr), or in a $N_2$-filled MBraun glove box with a high capacity recirculator (<1 ppm $O_2$ and $H_2O$). Propylene (Matheson, polymerization grade) was purified by passage through a supported MnO $O_2$-removal column and an activated Davison 4 A molecular sieve column. Toluene was dried using an activated alumina column and Q-5 columns and then vacuum-transferred from Na/K alloy and stored in Teflon-valve sealed bulbs.[42] Al ($d$ = 140 nm) nanoparticles with a 2 nm native $Al_2O_3$ coating were purchased from Aldrich. The nanoparticles were then dried on a high vacuum line ($10^{-5}$ Torr) at 80 °C overnight to remove the surface-bound water. The reagent [*rac*-ethylenebisindenyl]zirconium dichloride was purchased from Sigma-Aldrich and used as received. Methylaluminoxane, 10% solution in toluene, was purchased from Sigma-Aldrich and purified by removing all the volatiles in vacuo. Aluminum substrates were purchased from McMaster-Carr (Chicago, IL) and cleaned according to standard procedures.[43]

*Physical and Analytical Measurements*: Elemental analyses were performed by Midwest Microlabs, LLC, Indianapolis, IN. Inductively coupled plasma-optical emission spectroscopy (ICP-OES) analyses were performed by Galbraith Laboratories, Inc., Knoxville, Tennessee. Transmission electron microscopy was performed on a Hitachi H-8100 TEM with an accelerating voltage of 200 kV.

The nanocomposite dielectric thin films for low frequency and high field measurements were fabricated on Al substrates by hot pressing at 130 °C and 1500 psi pressure. Post-pressing vacuum treatment at 80 °C was performed on all samples overnight to remove any residual moisture and trapped air bubbles. Parallel-plate capacitors were fabricated by vapor-depositing gold electrodes on the nanocomposite films. The thicknesses of the films were measured on a Veeco Dektak 150 surface profiler. The film morphologies were examined with a LEO1525 scanning electron microscope using an accelerating voltage of 3 kV after coating with 6 nm osmium using a SPF osmium coater. Film topography and RMS roughnesses were imaged using a JEOL SPM atomic force microscope.

*Nanocomposite Electrical Measurements*: Gold electrodes for metal-insulator-metal (MIM) devices were vacuum-deposited through shadow masks at (3-4) × $10^{-7}$ Torr (500 Å, 0.2–1.0 Å/s). A digital capacitance meter (Model 3000, GLK Instruments, San Diego CA) was used for capacitance measurements. Polarization measurements for recoverable energy storage were taken at 500 Hz on a locally fabricated high voltage system. Low frequency-dependent (≤1 MHz) capacitance and loss tangent were measured on an HP 4384A precision multimeter. Leakage current measurements were performed using a Keithley 6430 sub-femtoamp remote source meter using a locally written LABVIEW program. All of the above electrical characterizations were performed under ambient conditions in air.

*Immobilization of Metallocene Catalysts on Nanoparticles*: In the glovebox, 2.0 g of nanoparticles, 200 mg of the metallocene precatalyst $EBIZrCl_2$, and 50 mL of toluene were loaded into a predried 200 mL flip-frit flask. The color of the particle suspension turned to light orange. The slurry was then subjected to alternating sonication and vigorous stirring overnight. The particles were then collected by filtration and washed with fresh toluene until the toluene remained colorless. The particles were dried on the high-vacuum line overnight and stored in the glovebox at –40 °C in the dark.

*Representative Synthesis of a Nanocomposite via In Situ Propylene Polymerization*: In the glovebox, a 250 mL round-bottom three-neck Morton flask, equipped with a large magnetic stirring bar, was charged with 50 mL of dry toluene, 200 mg of the above catalyst-functionalized nanoparticles, and 50 mg of MAO. The assembled flask was removed from the glovebox and the mixture was subjected to sonication and vigorous stirring for 30 min. The flask was then attached to a high vacuum line ($10^{-5}$ Torr), the catalyst slurry degassed, equilibrated at the desired reaction temperature using an external water bath, and saturated with 1.0 atm (pressure control using a mercury bubbler) of rigorously purified propylene while vigorously stirring. After a measured polymerization reaction time interval (increasing the reaction time results in lower particle loadings), the polymerization was quenched by the addition of 5 mL of methanol, and the reaction mixture was then poured into 800 mL of methanol. The composite was allowed to fully precipitate overnight and was then collected by filtration, washed with fresh methanol, and dried on the high vacuum line at 80 °C overnight to constant weight.

## Supporting Information

Supporting Information is available from the Wiley Online Library or from the author.

## Acknowledgements

This research was supported by ONR (MURI N00014-05-1-0766; capacitor materials characterization) and by DOE (DE-FG02-86ER13511;

supported polymerization catalysis and energy storage). The project made use of Central Facilities supported by the NSF MRSEC program (DMR-1121262) at the Materials Research Center of Northwestern U. We thank J. Long and the equipment staff at Penn State U. for all their assistance with the high field polarization measurements.

Received: August 29, 2012
Revised: December 19, 2012
Published online: February 7, 2013

[1] a) M. Mackey, A. Hiltner, E. Baer, L. Flandin, M. A. Wolak, J. S. Shirk, *J. Phys. D: Appl. Phys.* **2009**, *42*, 175304; b) Y. Han, F. Lin, L. Dai, H. Li, L. Wang, L. Bo, Z. Long, B. Peng, *IEEE Trans. Dielectr. Electr. Insul.* **2009**, *16*, 979; c) R. M. Wallace, G. D. Wilk, *Crit. Rev. Solid State Mater. Sci.* **2003**, *28*, 231; d) K. M. Slenes, P. Winsor, T. Scholz, M. Hudis, *IEEE Trans. Magn.* **2001**, *37*, 324.

[2] a) J. Pan, K. Li, J. Li, T. Hsu, Q. Wang, *Appl. Phys. Lett.* **2009**, *95*, 022902; b) J. Claude, Y. Lu, K. Li, Q. Wang, *Chem. Mater.* **2008**, *20*, 2078; c) Y. Cao, P. C. Irwin, K. Younsi, *IEEE Trans. Dielectr. Electr. Insul.* **2004**, *11*, 797; d) *Handbook of Low and High Dielectric Constant Materials and their Applications* (Ed: H. S. Nalwa), Academic Press, New York **1999**.

[3] a) Q. Wang, L. Zhu, *J. Polym. Sci., Part B: Polym. Phys.* **2011**, *49*, 1421; b) H. Fricke, *J. Phys. Chem.* **1953**, *57*, 934.

[4] a) M. A. Ordal, R. J. Bell, J. R. W. Alexander, L. L. Long, M. R. Querry, *Appl. Opt.* **1985**, *24*, 4493; b) K. Tanabe, *J. Phys. Chem. C* **2008**, *112*, 15721; c) A. J. Pointon, K. F. Woodman, *J. Phys. E: Sci. Inst.* **1971**, *4*, 208.

[5] a) Z. M. Dang, J. B. Wu, L. Z. Fan, C. W. Nan, *Chem. Phys. Lett.* **2003**, *376*, 389; b) Z.-M. Dang, Y.-H. Lin, C.-W. Nan, *Adv. Mater.* **2003**, *15*, 1625.

[6] a) P. Michalczyk, M. Bramoulle, *IEEE Trans. Magn.* **2003**, *39*, 362; b) M. Rabuffi, G. Picci, *IEEE Trans. Plasma Sci.* **2002**, *30*, 1939.

[7] a) L. A. Fredin, Z. Li, M. T. Lanagan, M. A. Ratner, J. Marks Tobin, *Adv. Mater.* **2012**, *24*, 5946; b) J. Li, S. I. Seok, B. Chu, F. Dogan, Q. Zhang, Q. Wang, *Adv. Mater.* **2009**, *21*, 217.

[8] a) P. Kim, N. M. Doss, J. P. Tillotson, P. J. Hotchkiss, M.-J. Pan, S. R. Marder, J. Li, J. P. Calame, J. W. Perry, *ACS Nano* **2009**, *3*, 2581; b) J. Li, S. I. Seok, B. Chu, F. Dogan, Q. Zhang, Q. Wang, *Adv. Mater.* **2009**, *21*, 217; c) J. Li, J. Claude, L. E. Norena-Franco, S. I. Seok, Q. Wang, *Chem. Mater.* **2008**, *20*, 6304; d) S. Gross, D. Camozzo, V. Di Noto, L. Armelao, E. Tondello, *Eur. Polym. J.* **2007**, *43*, 673; e) T. Tanaka, G. C. Montanari, R. Mülhaupt, *IEEE Trans. Dielectr. Electr. Insul.* **2004**, *11*, 763.

[9] M. Lines, A. Glass, *Principles and Applications of Ferroelectrics and Related Materials*, Clarendon, Oxford **1977**.

[10] Z.-M. Dang, J.-K. Yuan, J.-W. Zha, T. Zhou, S.-T. Li, G.-H. Hu, *Profg. Mater. Sci.* **2012**, *57*, 660.

[11] Y. Bai, Z. Y. Cheng, V. Bharti, H. S. Xu, Q. M. Zhang, *Appl. Phys. Lett.* **2000**, *76*, 3804.

[12] a) H. Fricke, *Phys. Rev.* **1924**, *24*, 575; b) W. Xia, Z. Xu, F. Wen, Z. Zhang, *Ceram. Int.* **2012**, *38*, 1071; c) V. Tomer, E. Manias, C. A. Randall, *J. Appl. Phys.* **2011**, *110*, 044107; d) Y. Wang, X. Zhou, Q. Chen, B. Chu, Q. Zhang, *IEEE Trans. Dielectr. Electr. Insul.* **2010**, *17*, 1036; e) H. Ogihara, C. A. Randall, S. Trolier-McKinstry, *J. Am. Ceram. Soc.* **2009**, *92*, 1719; f) J.-K. Yuan, Z.-M. Dang, S.-H. Yao, J.-W. Zha, T. Zhou, S.-T. Li, J. Bai, *J. Mater. Chem.* **2010**, *20*, 2441.

[13] a) Y. Kobayashi, T. Tanase, T. Tabata, T. Miwa, M. Konno, *J. Eur. Ceram. Soc.* **2008**, *28*, 117; b) Z.-M. Dang, H.-P. Xu, H.-Y. Wang, *Appl. Phys. Lett.* **2007**, *90*, 012901; c) R. Schroeder, L. A. Majewski, M. Grell, *Adv. Mater.* **2005**, *17*, 1535.

[14] a) P. Kim, S. C. Jones, P. J. Hotchkiss, J. N. Haddock, B. Kippelen, S. R. Marder, J. W. Perry, *Adv. Mater.* **2007**, *19*, 1001; b) S. Ramesh, B. A. Shutzberg, C. Huang, J. Gao, E. P. Giannelis, *IEEE Trans. Adv. Packag.* **2003**, *26*, 17.

[15] M. Roy, J. K. Nelson, R. K. MacCrone, L. S. Schadler, C. W. Reed, R. Keefe, W. Zenger, *IEEE Trans. Dielectr. Electr. Insul.* **2005**, *12*, 629.

[16] a) N. Guo, S. A. DiBenedetto, P. Tewari, M. T. Lanagan, M. A. Ratner, T. J. Marks, *Chem. Mater.* **2010**, *22*, 1567; b) Z. Li, L. A. Fredin, P. Tewari, S. A. DiBenedetto, M. T. Lanagan, M. A. Ratner, T. J. Marks, *Chem. Mater.* **2010**, *22*, 5154; c) N. Guo, S. A. DiBenedetto, D.-K. Kwon, L. Wang, M. T. Russell, M. T. Lanagan, A. Facchetti, T. J. Marks, *J. Am. Chem. Soc.* **2007**, *129*, 766.

[17] a) W. Kaminsky, A. Funck, K. Wiemann, *Macromol. Symp.* **2006**, *239*, 1; b) K.-T. Li, Y.-T. Kao, *J. Appl. Polym. Sci.* **2006**, *101*, 2573; c) G. Fink, B. Steinmetz, J. Zechlin, C. Przybyla, B. Tesche, *Chem. Rev.* **2000**, *100*, 1377.

[18] a) T. J. Marks, *Proc. Natl. Acad. Sci. USA* **2006**, *103*, 15288; b) N. Suzuki, *Top. Organomet. Chem.* **2005**, *8*, 177; c) W. Kaminsky, *J. Polym. Sci., Part A Polym. Chem.* **2004**, *42*, 3911; d) W. Kaminsky, *Applied Homogeneous Catalysis with Organometallic Compounds*, Wiley-VCH, Weingheim, Germany **2002**; e) S. Lin, R. M. Waymouth, *Acc. Chem. Res.* **2002**, *35*, 765; f) T. J. Marks, *Acc. Chem. Res.* **1992**, *25*, 57.

[19] E. Y.-X. Chen, T. J. Marks, *Chem. Rev.* **2000**, *100*, 1391.

[20] a) P. Gonon, A. Boudefel, *J. Appl. Phys.* **2006**, *99*, 024308/1; b) L. Qi, B. I. Lee, S. Chen, W. D. Samuels, G. J. Exarhos, *Adv. Mater.* **2005**, *17*, 1777; c) C. Pecharroman, J. S. Moya, *Adv. Mater.* **2000**, *12*, 294; d) R. Fisch, A. B. Harris, *Phys. Rev. B* **1978**, *18*, 416.

[21] D. M. Grannan, J. C. Garland, D. B. Tanner, *Phys. Rev. Lett.* **1981**, *46*, 375.

[22] C. Nan, *Prog. Mater. Sci.* **1993**, *37*, 1.

[23] a) X. Huang, P. Jiang, C. Kim, Q. Ke, G. Wang, *Compos. Sci.Technol.* **2008**, *68*, 2134; b) N. Gascoin, P. Gillard, G. Baudry, J. Hazard, *Materials* **2009**, *171*, 348.

[24] a) X. Y. Huang, P. K. Jiang, C. U. Kim, *J. Appl. Phys.* **2007**, *102*, 124103/1; b) R. E. Dutton, M. N. Rahaman, *J. Mater. Sci. Lett.* **1993**, *12*, 1453; c) Z.-M. Dang, J.-P. Wu, H.-P. Xu, S.-H. Yao, M.-J. Jiang, J. Bai, *Appl. Phys. Lett.* **2007**, *91*, 072912.

[25] Z. Yang, J. Chen, L. He, H. Cong, H. Ye, *Acta Mater.* **2009**, *57*, 3633.

[26] a) L. A. Williams, T. J. Marks, *Organometallics* **2009**, *28*, 2053; b) S. B. Amin, T. J. Marks, *Angew. Chem., Int. Ed.* **2008**, *47*, 2006; c) G. Alt Helmut, *Dalton Trans.* **2005**, 3271; d) C. Coperet, M. Chabanas, R. P. Saint-Arroman, J.-M. Basset, *Angew. Chem. Int. Ed.* **2003**, *42*, 156; e) W. Wang, L. Wang, *J. Polym. Mater.* **2003**, *20*, 1; f) O. Delacroix, J. A. Gladysz, *Chem. Commun.* **2003**, 665; g) G. G. Hlatky, *Chem. Rev.* **2000**, *100*, 1347; h) L. Reven, *J. Mol. Catal.* **1994**, *86*, 447.

[27] S. L. Wegener, T. J. Marks, P. C. Stair, *Acc. Chem. Res.* **2011**, *45*, 206.

[28] a) Y. Shen, Y. Lin, M. Li, C.-W. Nan, *Adv. Mater.* **2007**, *19*, 1418; b) S. Gam, J. S. Meth, S. G. Zane, C. Chi, B. A. Wood, K. I. Winey, N. Clarke, R. J. Composto, *Soft Matter* **2012**, *8*, 6512; c) J. Li, P. Khanchaitit, K. Han, Q. Wang, *Chem. Materials* **2010**, *22*, 5350.

[29] D. Toker, D. Azulay, N. Shimoni, I. Balberg, O. Millo, *Phys. Rev. B* **2003**, *68*, 041403.

[30] a) V. Tomer, G. Polizos, C. A. Randall, E. Manias, *J. Appl. Phys.* **2011**, *109*, 074113; b) W. Xia, J. Li, Z. Zhang, Z. Xu, *Ferroelectrics* **2010**, *407*, 125.

[31] a) Z. Xin, C. Baojin, B. Neese, L. Minren, Q. M. Zhang, *IEEE Trans. Dielectr. Electr. Insul.* **2007**, *14*, 1133; b) S. A. Paipetis, G. M. Tsangaris, J. M. Tsangaris, *Polym. Commun.* **1983**, *24*, 373; c) A. Huzayyin, S. Boggs, R. Ramprasad, *IEEE Trans. Dielectr. Electr. Insul.* **2010**, *17*, 926; d) S. Boggs, *IEEE Trans. Dielectr. Electr. Insul.* **2005**, *12*, 929.

[32] K. Zhou, S. A. Boggs, R. Ramprasad, M. Aindow, C. Erkey, S. P. Alpay, *Appl. Phys. Lett.* **2008**, *93*, 102908.

[33] a) L. Qi, B. I. Lee, S. Chen, W. D. Samuels, G. J. Exarhos, Adv. Mater. **2005**, *17*, 1777; b) R. Yang, C. P. Wong, in *Proc. Electronic*

*Components and Technology Conference*, *52nd*, San Diego, CA, USA **2002** 920–923.

[34] C. Sung-Dong, P. Kyung-Wook, in *Proc. Electronic Components and Technology Conference*, *51st*, Orlando, FL, USA **2001** 1418–1422.

[35] a) A. B. Afzal, M. J. Akhtar, M. Nadeem, M. M. Hassan, *Curr. App. Phys.* **2010**, *10*, 601; b) I. Ben Amor, H. Rekik, H. Kaddami, M. Raihane, M. Arous, A. Kallel, *J. Electrost.* **2009**, *67*, 717.

[36] R. Popielarz, C. K. Chiang, R. Nozaki, J. Obrzut, *Macromolecules* **2001**, *34*, 5910.

[37] J. Xu, C. P. Wong, *Appl. Phys. Lett.* **2005**, *87*, 082907/1.

[38] a) M. Barra, F. V. D. Girolamo, F. Chiarella, M. Salluzzo, Z. Chen, A. Facchetti, L. Anderson, A. Cassinese, *J. Phys. Chem. C* **2010**, *114*, 20387; b) M. Houssa, P. W. Mertens, M. M. Heyns, J. S. Jeon, A. Halliyal, B. Ogle, *Solid-State Electron.* **2000**, *44*, 521.

[39] L. Zhu, Q. Wang, *Macromolecules* **2012**, *45*, 2937.

[40] F.-C. Chen, C.-H. Liao, *Appl. Phys. Lett.* **2008**, *93*, 103310.

[41] F. Guan, L. Yang, J. Wang, B. Guan, K. Han, Q. Wang, L. Zhu, *Adv. Funct. Mater.* **2011**, *21*, 3176.

[42] A. B. Pangborn, M. A. Giardello, R. H. Grubbs, R. K. Rosen, F. J. Timmers, *Organometallics* **1996**, *15*, 1518.

[43] M.-H. Yoon, C. Kim, A. Facchetti, T. J. Marks, *J. Am. Chem. Soc.* **2006**, *128*, 12851.